Minimizing Scanning Errors in Piezoelectric Stack-Actuated Nanopositioning Platforms

Sumeet S. Aphale, Bharath Bhikkaji, and S. O. Reza Moheimani, *Senior Member, IEEE*

***Abstract*—Piezoelectric stack-actuated parallel-kinematic nanopositioning platforms are widely used in nanopositioning applications. These platforms have a dominant first resonant mode at relatively low frequencies, typically in the hundreds of hertz. Furthermore, piezoelectric stacks used for actuation have inherent nonlinearities such as hysteresis and creep. These problems result in a typically low-grade positioning performance. Closed-loop control algorithms have shown the potential to eliminate these problems and achieve robust, repeatable nanopositioning. Using closed-loop noise profile as a performance criterion, three commonly used damping controllers, positive position feedback, polynomial-based pole placement, and resonant control are compared for their suitability in nanopositioning applications. The polynomial-based pole placement controller is chosen as the most suitable of the three. Consequently, the polynomial-based control design to damp the resonant mode of the platform is combined with an integrator to produce raster scans of large areas. A scanning resolution of approximately 8 nm, over a 100 μm $\times$ 100 μm area is achieved.**

***Index Terms*—Feedback control, nanopositioning, resonance damping, tracking.**

I. Introduction

AS WE ENTER the age of miniaturization, the performance of nanomachinery is of ever-increasing importance. Nanopositioning is a key technology that impacts a range of important fields, including nanomachining, scanning probe microscopy, microlithography, and nanometrology [1]–[5]. There is an ever-present demand for nanopositioning systems that operate with higher resolution, greater accuracy, higher scanning speeds, and a larger range of motion. Although piezoelectric tube scanners continue to be widely used in such applications [6], [7], they are now being overtaken by piezoelectric stack-actuated nanopositioning platforms, due to their larger range of motion, greater mechanical robustness, and lower cross coupling between the axes. These platforms can also be easily integrated with existing scanning microscopes and these qualities have generated significant research aimed at improving their overall performance.

Resonant modes due to the mechanical construction and nonlinearities inherent to piezoelectric stack actuators, are the two main factors limiting the performance of these nanopositioning platforms. Techniques to damp the resonant modes of highly resonant systems such as piezoelectric tube nanopositioners have been proposed and documented by researchers in the past [8]. These techniques can also be applied to damp the resonance of platform nanopositioners. Damping techniques can be classified into two broad classes: active and passive. Passive techniques such as shunt damping have been reported by earlier researchers [9]. Although, such techniques can deliver acceptable performance, they may need frequent tuning [10]. For this reason active closed-loop control techniques are preferable. Model-based control techniques have been reported earlier [11]–[13]. Resonant control has been applied to damp resonant systems [14]. These controllers have attractive robustness properties. However, they also have a high-pass profile and may worsen the measurement noise, a main consideration in precise nanopositioning applications. Polynomial-based pole placement control [15], and positive position feedback (PPF) control [16], are other popular techniques that have shown the ability to damp the resonant modes. Polynomial-based pole placement has been applied to damp the resonant modes of nanopositioning systems such as the piezoelectric tube nanopositioners [17]. PPF control has been successfully used to damp the resonant modes of a cantilever beam [18]. These controllers provide robust damping performance under variations in resonance frequencies. Also, they roll off at high frequencies and thus do not excite high-frequency dynamics or worsen the noise profile.

Hysteresis and creep are the main nonlinearities associated with piezoelectric materials. In nanopositioning platforms actuated by piezoelectric stacks, these nonlinearities result in a degraded trace of the reference input. Charge actuation of a piezoelectric element has shown to reduce hysteresis by about 89%. As per the authors' knowledge, charge sources capable of supplying highly capacitive loads (to the tune of 10 μf, roughly the capacitance of the piezoelectric stacks) are not commercially available at present. Thus, closed-loop compensation of hysteresis with voltage actuation is desirable. To model hysteresis and alleviate the problems introduced due to it, many computationally intensive approaches have been formulated [19], [20]. Simple tracking controllers such as an integrator can result in eliminating errors due to hysteresis and creep [21].

Lower resolution due to fed-through noise is the main factor deeming the implementation of closed-loop nanopositioning schemes less common than the open-loop architectures [22]. Open-loop compensation for the vibration as well as nonlinearities in piezoelectric actuators has been proposed earlier [23]. Researchers have also proposed feedforward techniques to address hysteresis as well as simple filter based com-

Manuscript received June 26, 2007; revised September 20, 2007. This work was supported by the Australian Research Council's Center of Excellence for Complex Dynamic Systems and Control. The review of this paper was arranged by Associate Editor L. Dong.

The authors are with the School of Electrical Engineering and Computer Science, University of Newcastle, Callaghan NSW 2308, Australia (e-mail: Sumeet.Aphale@newcastle.edu.au; Bharath.Bhikkaji@newcastle.edu.au; Reza.Moheimani@newcastle.edu.au).

Color versions of one or more of the figures in this paper are available online at http://ieeexplore.ieee.org.

Digital Object Identifier 10.1109/TNANO.2007.910333

pensation techniques to deal with creep in piezoelectrically actuated scanning devices [24]–[26]. A point to note is that most high-resolution open-loop scans are either obtained for very small scan ranges ($< 10\ \mu$m) or at low speeds (<1 Hz). In this article, we propose a simple yet well-performing closed-loop nanopositioning scheme that results is large scans ($100\ \mu\text{m} \times 100\ \mu$m) at high speeds (4 Hz) and with a high resolution (8 nm).

A. Objectives

The main objective of this work is to obtain high-resolution closed-loop raster scans using a piezoelectric stack-actuated nanopositioning platform. The paper is organized as follows. Section II describes the experimental setup used in this work. Section III gives the details of the system identification and the design algorithms for the PPF, polynomial-based pole placement and resonant controllers. Detrimental impact of the measurement noise is the chief factor governing the implementation of closed-loop control in nanopositioning applications. Based on the noise analysis given in Section IV, it is decided that the polynomial-based pole placement control design is most suitable for this specific application. Section V presents the experimentally implemented polynomial-based pole placement controllers, the obtained minimization in hysteresis and creep as well as the closed-loop raster scans. Section VI concludes the paper.

II. Experimental Setup

The PI-734 nanopositioning platform, used in this work, is a two axis piezoelectric stack-actuated platform based on a parallel-kinematic design. This design provides mounting independent orthogonality and reduced cross coupling between the two axes. The platform has a flexure guidance system which eliminates friction and stiction. To increase the range of motion while maintaining the subnanometer accuracy of the platform, it is equipped with a built-in integrated lever motion amplifier (ILMA). Each axis of the nanopositioning platform is fitted with a two-plate capacitive sensor that provides a direct position measurement. Simplified diagrams of the nanopositioning platform, its components, and the ILMA are given in Fig. 1. The platform piezoelectric stack actuators take voltage input in the range of 0 V–100 V for each axis. The resultant motion produced by the platform is within 0 μm–100 μm. This motion is detected by the two-plate capacitive sensors and fed to an electronic sensor output module. The output of this module is within 0 V–6.7 V.

A dSPACE-1005 rapid prototyping system equipped with 16-bit ADC(DS2001)/DAC(DS2102) cards is used to implement the proposed control strategy. The sampling frequency of this system is 20 kHz. Fig. 2[1] shows the block diagram depicting the various gains associated with the system.

III. System Identification and Control

The nanopositioning platform is treated as a two-input two-output system. The inputs being voltage signals applied to the piezoelectric stacks in the X and Y directions (u in volts), and the outputs are the respective displacements (d in μm) obtained

[1]The notation given in this figure will be used throughout this paper for simplicity in understanding and consistency

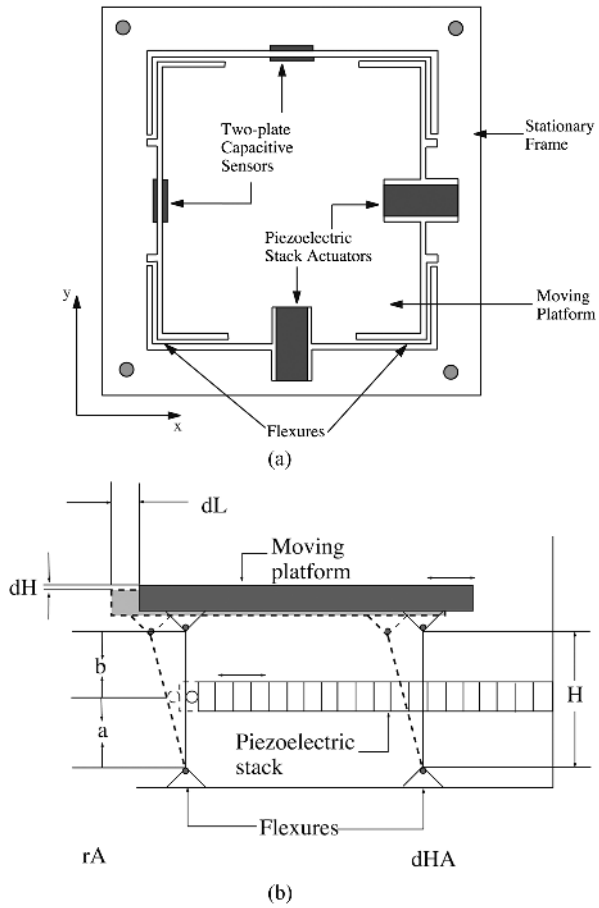

Fig. 1. (a) Working principle of the monolithic XY piezoelectric-stack actuated nanopositioning platform. (b) Basic parallelogram flexure guiding system with motion amplification. The amplification r (transmission ratio) is given by $r = (a + b/a)$ [27].

by scaling the measured capacitive sensor voltages by the proportional scaling factor (0.063 V/μm).

To identify the linear model within the bandwidth of interest and to minimize or eliminate the effects of nonlinearities such as hysteresis or creep, the plant was identified using a band-limited random noise input from an HP signal analyzer, of amplitude 1 Vpk within the frequency range of 10 Hz–810 Hz. This corresponds to 1 μm, or 1% of the total range of the platform. This small motion ensures that the nonlinear effects do not manifest in a dominant fashion. As the lowest frequency of interest at which the identification began was 10 Hz, the effect of creep was eliminated due to the absence of any low-frequency components.

A Laplace domain representation of this linear system is given by

$$Y(s) \triangleq G(s)U(s) \tag{1}$$

where $Y(s)$ and $U(s)$ are the Laplace transforms of the capacitive sensor outputs $[d_x, d_y]^\top$ and the input signals $[u_x, u_y]^\top$ respectively, and

$$G(s) = \begin{bmatrix} G_{\text{xx}}(s) & G_{\text{xy}}(s) \\ G_{\text{yx}}(s) & G_{\text{yy}}(s) \end{bmatrix} \tag{2}$$

is a 2×2 matrix of transfer functions.

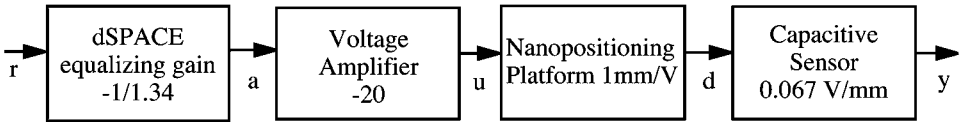

Fig. 2. Gains associated with the experimental setup; r is the reference input in volts, generated in dSPACE. a is the input to the amplifier in volts and u is the amplifier output in volts, used as the driving input for the nanopositioning platform; d is the actual displacement of the nanopositioning platform in μm and y is the proportionally scaled capacitive sensor output in volts. To get the overall output to input gain to be unity, an equalizing gain is introduced through the dSPACE.

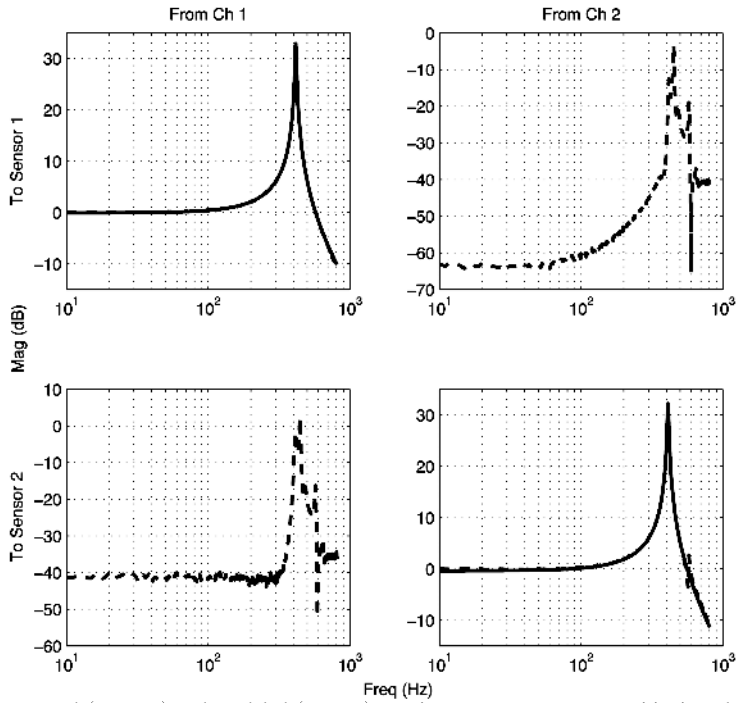

Fig. 3. Frequency response of the measured ($- - -$) and modeled (_____) two-input two-output nanopositioning platform from displacement output d to platform voltage input u, as mentioned in Fig. 2. Note that only the direct transfer functions G_{11} and G_{22} are modeled.

Determining the frequency response functions (FRFs) $G_{\rm xx}(i\omega)$ and $G_{\rm yx}(i\omega)$ boils down to applying an input of the form $[u_x, 0]$, and computing the ratios $G_{\rm xx}(i\omega) = (d_x(i\omega)/u_x(i\omega))$ and $G_{\rm yx}(i\omega) = (d_y(i\omega)/u_x(i\omega))$. Here, $u_x(i\omega), d_x(i\omega)$ and $d_y(i\omega)$ denote the Fourier transforms of u_x, d_x and d_y respectively. All the four FRFs, $G_{\rm xx}(i\omega)$ and $G_{\rm yx}(i\omega)$ obtained by applying an input $[u_x, 0]$, as well as $G_{\rm xy}(i\omega)$ and $G_{\rm yy}(i\omega)$ obtained by applying an input $[0, u_y]$, where u_x and u_y are random white noise signals generated using a spectrum analyzer, are plotted in Fig. 3. It must be mentioned here that the plots presented in Fig. 3 are averaged over several realizations of the input. The dominant first resonant modes for $G_{\rm xx}(i\omega)$ and $G_{\rm yy}(i\omega)$ occur at 410 and 415 Hz respectively. It is evident from Fig. 3 that the magnitude of the cross-coupling terms $G_{\rm xy}(i\omega)$ and $G_{\rm yx}(i\omega)$, at any $\omega > 0$, are less than the direct terms $G_{\rm xx}(i\omega)$ and $G_{\rm yy}(i\omega)$, respectively, by about 40 dB.[2] In other words the inputs u_x and u_y have negligible effect on the outputs d_y and d_x respectively. Hence, the system is assumed to be decoupled. Therefore, $G(s)$, (2), is approximated by

$$G(s) = \begin{bmatrix} G_{\rm xx}(s) & 0 \\ 0 & G_{\rm yy}(s) \end{bmatrix}. \tag{3}$$

As both $G_{\rm xx}(i\omega)$ and $G_{\rm yy}(i\omega)$, each have only one resonant mode in the bandwidth of interest, second-order models given by

$$G_{\rm xx}(s) = \frac{k_x}{s^2 + 2\sigma_x\omega_x s + \omega_x^2} + D_x \tag{4}$$

and

$$G_{\rm yy}(s) = \frac{k_y}{s^2 + 2\sigma_y\omega_y s + \omega_y^2} + D_y \tag{5}$$

accurately capture the dynamics of the measured FRFs for the measured frequency range. The parameters of these models are tabulated in Table I. As the models are of second order their estimation is not difficult, and the details on parameter estimation are omitted.[3]

A. Control Design

As the system is considered decoupled with the input u_x having negligible effect on the output d_y and *vice versa*, control systems can be designed independently for each axis. Here, a control system design of the form shown in Fig. 4 is presented for the actuation along the x axis. Control system design for actuation along the y axis is identical and therefore, is omitted for the sake of brevity.

[2]The two resonant modes seen in each of the cross-coupling FRFs are due to the mechanical resonant peaks of each individual axis. Therefore, they occur at exactly the same frequencies, i.e., at 410 and 415 Hz, in both the $G_{\rm xy}$ and $G_{\rm yx}$.

[3]The E-509 sensor conditioning unit introduces a small but significant delay (in the tune of 100 μs) into the measured system. Subspace-based modeling techniques [28]used to procure the system models introduce non-minimum phase zeros to account for this effect.

TABLE I
PARAMETER VALUES OF THE FRFS $G_{\rm xx}(s)$, $G_{\rm yy}(s)$, $G_{c_{\rm xx}}(s)$ AND $G_{c_{\rm yx}}(s)$

k_x	8.1532×10^6
$2\sigma_x\omega_x$	6.05×10^1
ω_x^2	6.65×10^6
D_x	-0.13
k_y	8.0023×10^6
$2\sigma_y\omega_y$	5.64×10^1
ω_y^2	6.8×10^6
D_y	-0.13

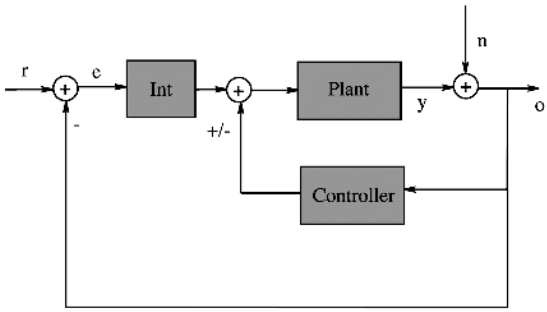

Fig. 4. Closed-loop block diagram with the sensor noise modeled as an output disturbance. Two of the proposed controllers are implemented in positive feedback, while the third in negative feedback. Hence, the $\pm$ sign in the internal loop.

In the control design presented in Fig. 4, controller $C_1(s)$ is aimed at damping the resonant mode of $G_{\rm xx}(s)$, while $C_2(s)$ is the integral controller incorporated to track the reference signal. In the following, three different control techniques, i) polynomial-based pole placement control (will be referred to as polynomial-based control, from now on); ii) PPF control; and iii) resonant control, will be used for deriving $C_1(s)$. The three controllers, one from each technique, will be derived such that they damp the resonant peak (magnitude of $G_{\rm xx}(s)$ at the resonance frequency) by approximately the same level. In Section IV, one of the three will be chosen based on their response to sensor noise $n(t)$, see Fig. 4.

1) Polynomial-Based Controller: In the current context, a polynomial-based controller is defined by the second-order transfer function

$$K_{\rm Poly}(s) \triangleq \frac{\Gamma_1 s + \Gamma_2}{s^2 + 2\xi w s + w^2} \tag{6}$$

where ξ, w, Γ_1 and Γ_2 are the design parameters. Since the feedback is positive, the transfer-function connecting the output d_x and the input u_x is given by

$$G_{\rm xx}^{(cl)}(s) = \frac{G_{\rm xx}(s)}{1 - G_{\rm xx}(s)K_{\rm Poly}(s)}. \tag{7}$$

It can be checked that poles of the closed-loop transfer function $G_{\rm xx}^{(cl)}(s)$, (7), are the roots of the polynomial

$$\begin{aligned} P(s) = {} & s^4 + (2\sigma_x\omega_x + (2\xi w - \Gamma_1 D_x))s^3 \\ & + \left(\omega_x^2 + 2\sigma_x\omega_x(2\xi w - \Gamma_1 D_x) + \left(w^2 - \Gamma_2 D_x\right)\right)s^2 \\ & + (2\sigma_x\omega_x(w^2 - \Gamma_2 D_x) + (2\xi w - \Gamma_1 D_x)\omega_x^2 - k_x\Gamma_1)s \\ & + \omega_x^2\left(w^2 - \Gamma_2 D_x\right) - k_x\Gamma_2. \end{aligned} \tag{8}$$

For the closed-loop system to be well damped, it is desirable to have the roots of the polynomial $P(s)$ well inside the left half plane. Assume that $\{p_i\}_{i=1}^4$ are the desired pole positions of the closed-loop system and

$$Q(s) \triangleq s^4 + K_1 s^3 + K_2 s^2 + K_3 s + K_4 \tag{9}$$

is the corresponding polynomial with roots $\{p_i\}_{i=1}^4$. Matching the coefficients of $P(s)$ and $Q(s)$ would give

$$2\sigma_x\omega_x + 2\xi w - \Gamma_1 D_x = K_1 \tag{10}$$

$$\omega_x^2 + 2\sigma_x\omega_x(2\xi w - \Gamma_1 D_x) + \left(w^2 - \Gamma_2 D_x\right) = K_2 \tag{11}$$

$$2\sigma_x\omega_x\left(w^2 - \Gamma_2 D_x\right) + (2\xi w - \Gamma_1 D_x)\omega_x^2 - k_x\Gamma_1 = K_3 \tag{12}$$

and

$$\omega_x^2\left(w^2 - \Gamma_2 D_x\right) - k_x\Gamma_2 = K_4. \tag{13}$$

Note that (10)–(13) are linear in $2\xi w$, w^2, Γ_1 and Γ_2, and can be solved for them to obtain the controller $K_{\rm Poly}(s)$. However, for the controller $K_{\rm Poly}(s)$ to be stable, or even meaningful, the quantities $2\xi w$ and w^2, have to be positive. Therefore, the desired polynomial coefficients K_1, K_2, K_3, and K_4 have to be such that (10)–(13) yield positive solutions for $2\xi w$ and w^2. For one axis, the polynomial-based controller design is described below. Note that poles of $G_{\rm xx}(s)$, computed from (4), are

$$p_\pm = -30.23 \pm i2578.5. \tag{14}$$

Here, the desired closed-loop poles are set to

$$\begin{aligned} P_{1+} = P_{2+} &= -1030.23 \pm i2578.5, \\ P_{1-} = P_{2-} &= -1030.23 \pm i2578.5 \end{aligned} \tag{15}$$

which amounts to placing the closed-loop poles of the system further into the left half plane by 1000 units. It can be checked that the polynomial coefficients corresponding to the desired poles (15) are $K_1 = 4.1209 \times 10^3$, $K_2 = 1.9666 \times 10^7$, $K_3 = 3.1773 \times 10^{11}$, and $K_4 = 5.9447 \times 10^{15}$.

Solving for the controller parameters Γ_1, Γ_2, ξ, and w from (10)–(13), gives the controller

$$K_{\rm Poly}(s) \triangleq \frac{-499.9s + 3.249.10^6}{s^2 + 4121s + 1.247 \times 10^7} \tag{16}$$

that would render a closed-loop system having poles at P_{1+}, P_{2+}, P_{1-}, and P_{2-}. This controller damps the resonant mode of the x axis by 23 dB as shown in Fig. 5(a).

2) PPF Controller: A PPF controller is defined by the second-order transfer function

$$K_{\rm PPF}(s) = \frac{\gamma_p}{s^2 + 2\eta_p\omega_p s + \omega_p^2}. \tag{17}$$

It is similar to polynomial-based controller, (6), but does not have the velocity term Γ_1. Since the feedback is positive, the transfer-function connecting the output d_x and the input u_x is given by

$$G_{\rm CL,xx}(s) = \frac{G_{\rm xx}(s)}{1 - K_{\rm PPF}(s)G_{\rm xx}(s)}. \tag{18}$$

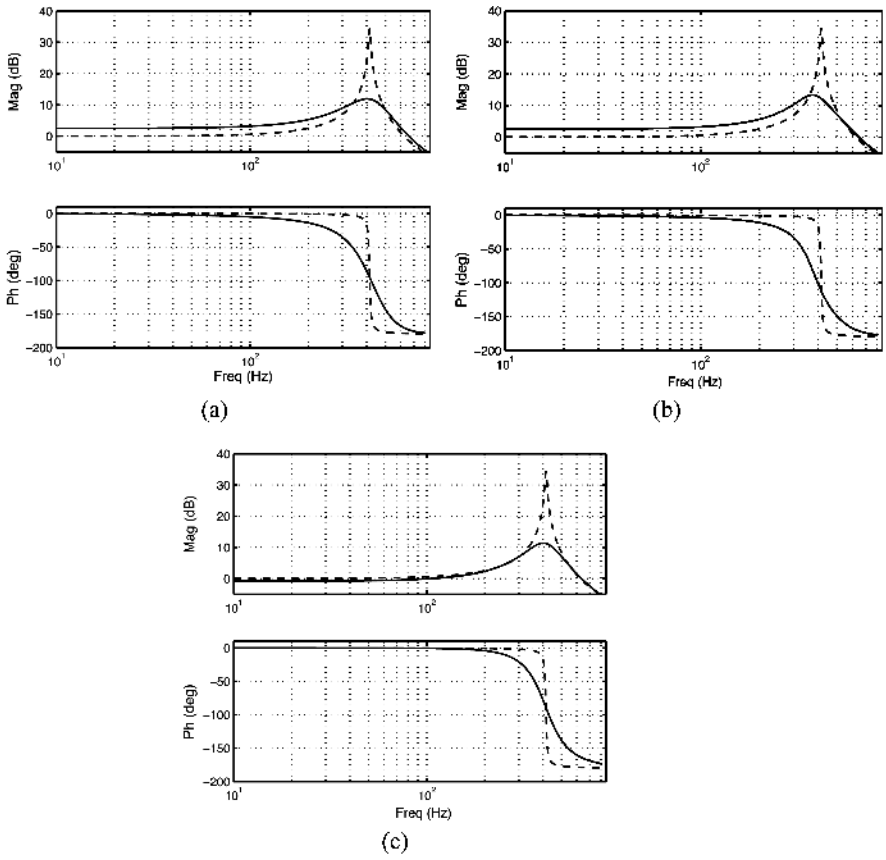

Fig. 5. Open-loop ($- - -$) and closed-loop (_____) frequency response of one axis of the nanopositioning platform damped using: (a) polynomial-based controller, (b) PPF controller, and (c) resonant controller.

It can be checked that the denominator polynomial of (18) is equal to

$$C(s) \triangleq \left(s^2 + 2\sigma_x\omega_x s + \omega^2\right)\left(s^2 + 2\eta_p\omega_p s + \omega_p^2\right) - \gamma_p\left(k_x + D_x\left(s^2 + 2\sigma_x\omega_x s + \omega_x^2\right)\right). \quad (19)$$

Assuming that the desired closed-loop polynomial is as in (9), and matching the coefficients of (19) and (9) gives

$$2\eta_p\omega_p = K_1 - 2\sigma_x\omega_x \quad (20)$$

$$\omega_p^2 + 2\sigma\omega 2\eta_p\omega_p - D_x\gamma_p = K_2 - \omega_x^2 \quad (21)$$

$$\omega_x^2 2\eta_p\omega_p + \omega_p^2 2\sigma_x\omega_x - D_x 2\sigma_x\omega_x\gamma_p = K_3 \quad (22)$$

$$\omega_x^2\omega_p^2 - (k_x + D_x\omega_x^2)\gamma_p = K_4. \quad (23)$$

Note that (20)–(23) can be written in the matrix form

$$Ax = b \quad (24)$$

where A is a 4×3 matrix with known elements, $x = \left(\gamma_p, \omega_p^2, 2\eta_p\omega_p\right)^\top$ is a vector of control parameters, that need to determined, and $b = \left[K_1 - 2\sigma_x\omega_x, K_2 - \omega_x^2, K_3, K_4\right]^\top$. If b does not lie in the column space of A, i.e., $b \notin \text{Col}(A)$, then a solution for (24) will not exist. In which case, the vector b will be projected into $\text{Col}(A)$, and the parameter vector x will have to be solved by replacing b with $\hat{b}$ in (24). However, not all projections $\hat{b} \triangleq \left[\hat{K}_1, \hat{K}_2, \hat{K}_3, \hat{K}_4\right]$ of b will lead to stable closed loops. In other words, the closed-loop polynomial

$$\hat{Q}(s) = s^4 + \hat{K}_1 s^3 + \hat{K}_2 s^2 + \hat{K}_3 s + \hat{K}_4 \quad (25)$$

may not have all its roots in the left half plane. For the projected vector $\hat{b}$ to have stable polynomial coefficients, its components must have to satisfy the following constraints:

$$\hat{K}_1 > 0 \quad (26)$$

$$\hat{K}_2 > 0 \quad (27)$$

$$\hat{K}_3 > 0 \quad (28)$$

$$\hat{K}_4 > 0 \quad (29)$$

and

$$\hat{K}_4\hat{K}_1^2 + \hat{K}_3\left(\hat{K}_3 - \hat{K}_2\hat{K}_1\right) < 0. \quad (30)$$

Inequality (30) is obtained using the standard routh criterion. Since $\hat{K}_1$, $\hat{K}_2$, $\hat{K}_3$, and $\hat{K}_4$ are obtained by projecting b onto the column space of A, it is easy to see that $\hat{K}_i = A_i x$, where A_i denotes the ith row of A. Therefore, the inequalities (26)–(29) can be expressed as linear inequalities in the controller parameters. And by the same argument (30) can be expressed as a non-linear inequality in the controller parameters. Hence, a formal treatment of determining x would involve minimizing $\| Ax - b \|$, under three liner constraints and one non-linear constraint. Solving this optimization problem is not simple as (30) is nonconvex.

Here, we aspire for a PPF controller K_{PPF}, which gives the same level of damping as the controller K_{Poly}, (16), designed earlier. The structures of the PPF and polynomial-based controllers differ only by an extra parameter Γ_1. Since, in

(16)$|\Gamma 1| \ll |\Gamma_2|$, the effect of Γ_1 is negligible near the low frequency regions. Thus, a PPF controller with Γ_1 set zero in (16) would behave the same way as (16) near the low frequency regions. Therefore, here Γ_1 is set to zero and the resulting PPF controller

$$K_{\mathrm{PPF}}(s) \triangleq \frac{3.249.10^6}{s^2 + 4121s + 1.247.10^7} \tag{31}$$

is tested to determine if it gives the same level of damping as (16), and also renders the closed-loop system stable. In Fig. 5(b) frequency response of the closed-loop system, obtained using the $K_{\mathrm{PPF}}(s)$, (31), is plotted along with the open-loop system's frequency response. It can be noted by comparing Fig. 5(a) and (b), that both the polynomial-based and the PPF controllers give the same level of damping.

3) Resonant Controller: Resonant controllers approximate a differentiator over a narrow bandwidth, around the resonance frequencies of the structure to be damped. Damping is achieved by shifting the closed-loop poles of the system deeper into the left-half plane (LHP). In the current context, resonant controllers can be parametrized as

$$K_{\mathrm{Res}}(s) = \sum_{i=1}^{N} \frac{\alpha_i s^2}{s^2 + 2\delta_i \omega_i s + \omega_i^2} \tag{32}$$

where α_i, β_i, δ_i, and ω_i are the design parameters and N is the number of modes that need to be controlled [14]. The parametric form of the transfer function clearly shows the high-pass nature of the resonant controller. This will intuitively have an adverse effect on the closed-loop sensor noise to output characteristics as shown Section IV.

As only the dominant first resonant mode needs to be damped, N is set to 1, which implies

$$K_{\mathrm{Res}}(s) = \frac{\alpha s^2}{s^2 + 2\delta\omega s + \omega^2}. \tag{33}$$

As $K_{\mathrm{Res}}(s)$ is targeted to damp first resonant mode of the nanopositioning platform, the values of ω is set to the first resonance frequency of the platform. The values of α and δ are chosen using an approach similar to the one explained in [14]. The aim was to push the closed-loop poles of the system such that resonance of the nanopositioning platform is damped by approximately the same amount as that achieved by the PPF and the polynomial-based controllers. The transfer function of the resulting resonant controller can be written as

$$K_{\mathrm{Res}}(s) \triangleq \frac{0.3s^2}{s^2 + 3094s + 6.649 \times 10^6}. \tag{34}$$

Note that both PPF and polynomial-based controllers are implemented in positive feedback while the resonant controller is implemented in negative feedback. The three controllers discussed above were designed to damp the dominant resonant mode of the nano-positioning platform by 23 dB. It is seen from Fig. 5, that the PPF controller also increases the overall gain of the closed-loop system more than the polynomial-based controller or the resonant controller.

In Section IV, measurement noise is statistically analyzed. Using this analysis as a measure of accurate closed-loop nanopositioning, the effect of the three controllers presented earlier is evaluated and the controller best suited for nanopositioning applications is identified.

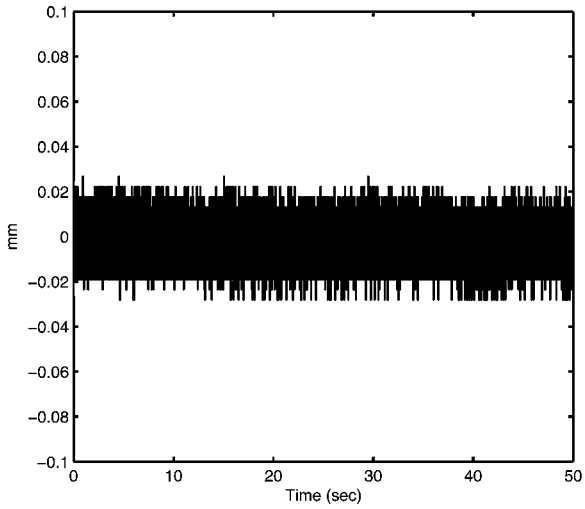

Fig. 6. Noise contribution due to the sensor conditioning electronics module E-509.

IV. Measurement Noise

Measurement noise is a major consideration in precision motion at nanometer scales. Though the two-plate capacitive sensors are capable of accurately sensing motion as small as 1 nm, the accompanying conditioning electronics adds noise to the measured position output and reduces the achievable resolution. Also, as this noise gets fed-back into the closed-loop system, it adversely affects the achievable resolution further. With this motivation, a detailed analysis of the measurement noise is performed in this section.

A metal plate was designed such that it rigidly bolts the moving nanopositioning platform to its stationary base (refer to Fig. 1). This results in the two plates of the capacitive sensor being exactly stationary with respect to each other. In this configuration the signal measured at the sensor output terminal of the E-509 is totally due to the noise contribution of the conditioning electronics in the module. Fig. 6 shows the recorded signal converted to μm. The sensor noise as well as the quantization noise are clearly visible in Fig. 6. In our setup, quantization error is not a major consideration as it is lower $(\approx$ 1 nm$)$ than the actual sensor noise $(\approx$ 9 nm$)$. A detailed statistical analysis of this sensor noise follows in Section IV-A.

The transfer function relating the actual system output y to the sensor noise n is calculated for the three controllers designed in Section III-A. Fig. 7 shows the FRF y/n for the three controllers. It can be seen that the PPF controller has the fastest roll-off characteristic and attenuates noise at all other frequencies except those near the resonance. At frequencies close to resonance, the input is amplified and is clearly seen in Fig. 7(b). Thus, this controller is not suitable for this specific application. The resonant controller has a high-pass characteristic and thus it propagates the input noise to the output with minimal attenuation, see Fig. 7(c). The polynomial-based controller does not amplify the noise at any frequency and its quick roll-off,

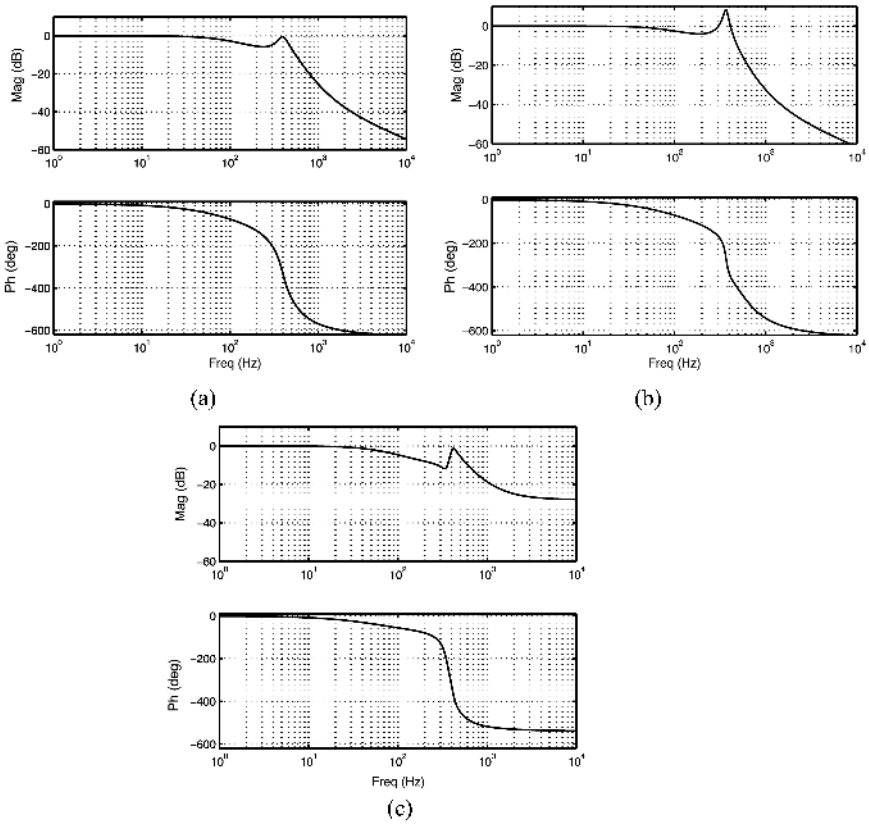

Fig. 7. Transfer functions relating the actual system output y to the sensor noise n. (a) Polynomial-based controller. (b) PPF controller. (c) Resonant controller.

at frequencies greater than the resonance, makes it ideal for closed-loop nanopositioning applications, see Fig. 7(a).

A. Noise Characterization

It can be verified that for the system illustrated in Fig. 4, the Laplace transform of the plant output $y(t)$ is equal to

$$\begin{aligned} Y(s) &= \frac{G(s)C_2(s)}{1+G(s)\left(C_2(s)-C_1(s)\right)}R(s) \\ &\quad - \frac{G(s)\left(C_2(s)-C_1(s)\right)}{1+G(s)\left(C_2(s)-C_1(s)\right)}N(s) \\ &\triangleq Y_r(s) - Y_n(s) \end{aligned} \tag{35}$$

where $G(s)$ denotes the plant dynamics, $C_1(s)$, and $C_2(s)$ denote the polynomial-based controller and the integral controller respectively, while $R(s)$ and $N(s)$ are Laplace transforms of the reference signal $r(t)$ and noise $n(t)$ respectively. When operating in open loop, where $Y(s) = G(s)R(s)$, the sensor noise does not disturb the actuation of the plant. However, in closed loop, the sensor noise is fed back into the system, leading to an additional term $Y_n(s)$, which is referred to as the noise response. In an ideal scenario, when the sensor noise $n(t) = 0$, the noise response $Y_n(s)$ would also be zero. Under normal circumstances, however, the noise response is the price to be paid for having a feedback loop, which is needed to deal with the adverse effects of creep, hysteresis, and vibration. As the sensor noise $n(t)$ is treated as a random variable, the system response $y(t)$, which is the inverse Laplace transform of $Y(s)$, is also a random variable. In the following, the empirical means of $n(t)$ and $y(t)$ and the empirical variance of $n(t)$ will be determined. A scheme for determining the empirical variance of $y(t)$ will also be presented. This scheme will be used in Section V.

In Fig. 8, a realization of $n(t)$, sampled at a rate $h = 5\times10^{-5}$, is plotted as an histogram. It can be noted from this figure that $|n(t)| < 0.04\ \mu$m, and the histogram closely resembles a normal density function. Here, the sensor noise $n(t)$ is assumed to be both stationary and ergodic, [29]. Therefore, its mean, variance and covariances can be approximated by

$$\begin{aligned} \hat{m}_n &= \frac{1}{N}\sum_{m=0}^{N-1} n(mh) \\ &\approx 0 \end{aligned} \tag{36}$$

$$\begin{aligned} \hat{\sigma}_n^2 &= \frac{1}{N}\sum_{m=0}^{N-1} n^2(mh) \\ &\approx 6.2287\times10^{-5}\ \mu\text{m}^2 \end{aligned} \tag{37}$$

and

$$\hat{R}_n(\tau_k) = \frac{1}{N}\sum_{m=0}^{N-1} n(mh)n((k+m)h) \tag{38}$$

where $\tau_k = kh$, and $k = 0, 1, 2, \ldots$, for a large N. Note that $\hat{R}(0) = \hat{\sigma}_n^2$.

Since the mean of $n(t)$ is approximately zero, due to linearity, the mean m_{y_n} of the noise response $y_n(t)$ (the inverse Laplace transform of $Y_n(s)$) must also be close to zero, [29]. In order to determine the variance of $y_n(t)$, the following relationship can be used:

$$S_{y_n}(i\omega) = |G_n(i\omega)|^2 S_n(i\omega) \tag{39}$$

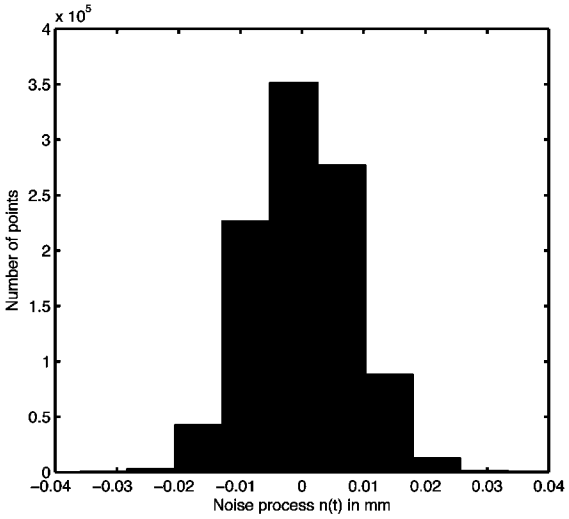

Fig. 8. Histogram plot of the noise process $n(t)$ for a realization.

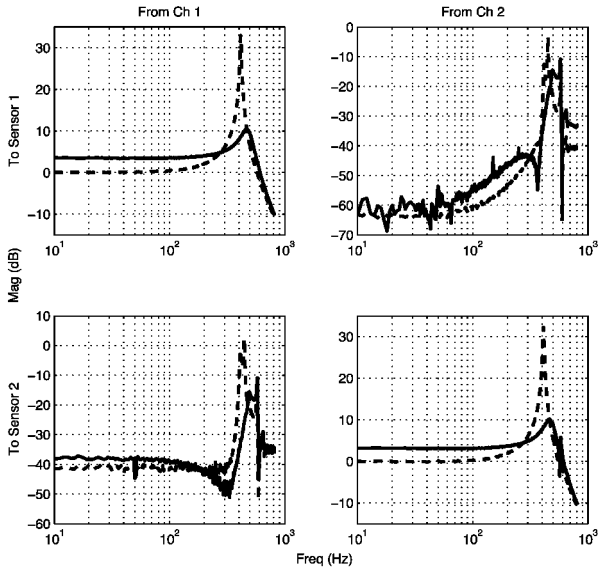

Fig. 9. Open-loop ($- - -$) and closed-loop with polynomial-based controller ($\_\_\_\_\_$) frequency responses of the two-input two-output nanopositioning platform from displacement output d to platform voltage input u, as denoted in Fig. 2.

where $S_n(i\omega)$ and $S_{y_n}(i\omega)$ are the spectral densities of $n(t)$ and $y_n(t)$ respectively and

$$G_n(i\omega) \triangleq \frac{G(i\omega)\left(C_2(i\omega) - C_1(i\omega)\right)}{1 + G(i\omega)\left(C_2(i\omega) - C_1(i\omega)\right)} \tag{40}$$

see also (35). The spectral density $S_x(i\omega)$ of a random variable $x(t)$ is the Fourier transform of its covariance function $R_x(\tau)$, [29]. Assuming that covariance $R_n(\tau)$ of $n(t)$ is band limited with the bandwidth being less than $|(\pi/h)|$, the spectral density $S_n(i\omega)$ of $n(t)$ can be well approximated by

$$\hat{S}_n(i\omega_k) = \sum_{m=-L}^{L} \hat{R}_n(\tau_m) e^{i\omega_k h} \tag{41}$$

where

$$\omega_k = \frac{\pi k}{Lh}, \quad k = -L, -(L-1), \ldots, 1, 0, 1, \ldots, L \tag{42}$$

and $\hat{R}_n(\tau_m)$ is as defined in (38). Using the relationship (39) an approximation

$$\hat{S}_{y_n}(i\omega_k) = |G_n(i\omega)|^2 \hat{S}_n(i\omega_k) \tag{43}$$

of the spectral density $S_{y_n}(i\omega)$ can be computed. Note that the inverse Fourier transform of $\left\{\hat{S}_{y_n}(i\omega_k)\right\}_{k=0}^{L-1}$ will give the covariance sequence $\left\{\hat{R}_{y_n}(\tau_k)\right\}_{k=0}^{L-1}$, from which the variance $\sigma_{y_n}^2 = \hat{R}_y n(0)$, of $y_n(t)$ can be determined.

V. Experimental Results Using the Polynomial-Based Controller

The polynomial-based controllers for the x and y axes are given by

$$K_{\mathrm{Poly}}(s) \triangleq \frac{-499.9s + 3.249.10^6}{s^2 + 4121s + 1.247.10^7} \tag{44}$$

and

$$K_{\mathrm{Poly}}(s) \triangleq \frac{-490.6s + 3.124 \times 10^6}{s^2 + 4124s + 1.237 \times 10^7} \tag{45}$$

respectively.

The effectiveness of the polynomial-based controller in damping the resonance of $G_{\mathrm{xx}}(s)$ is evaluated both numerically and experimentally. Evaluating numerically refers to using the expressions obtained for Γ_1, Γ_2, ξ, and ω in the closed-loop model (7) and determining the damping introduced by the controller. Evaluating experimentally refers to applying an input $[u_x\ 0]$, with u_x being a random white noise signal, and determining the FRF $G_{\mathrm{xx}}^{(cl)}(i\omega) = (d_x(i\omega)/u_x(i\omega))$ and the damping introduced by it. This is done to illustrate that the numerical predictions match the experimental results. Fig. 9 shows the experimentally measured frequency responses of the undamped and damped nanopositioning platform[4]. The plots presented in Fig. 9 have been averaged over several input realizations.

The nanopositioning platform has a relatively large range of motion (100 μm along each axis, X and Y). Piezoelectric stack-actuated platforms are prone to errors due to nonlinearities when moving about such large distances. To eliminate the problems associated with these nonlinearities, a suitable tracking controller is necessary [30]. An integral controller is a simple yet effective tracking controller and can easily be combined with the polynomial-based damping controller to result in a well-damped accurately tracking nanopositioning platform. The inner feedback loop (with the polynomial-based controller), imparts additional damping to the system and thus enables us to utilize a higher gain integral controller, which in turn delivers better tracking performance. Fig. 4 shows the complete control strategy implemented on one axis. The same is also duplicated on the other axis of the nanopositioning platform. A gain of 400 was deemed suitable for the integral control and this resulted in a stable closed-loop system with

[4]The cross-coupling FRFs G_{yx} and G_{xy} also show substantial damping at the resonances. Due to the low signal-to-noise ratio, good data at low frequencies could not be obtained for the cross-coupling FRFs

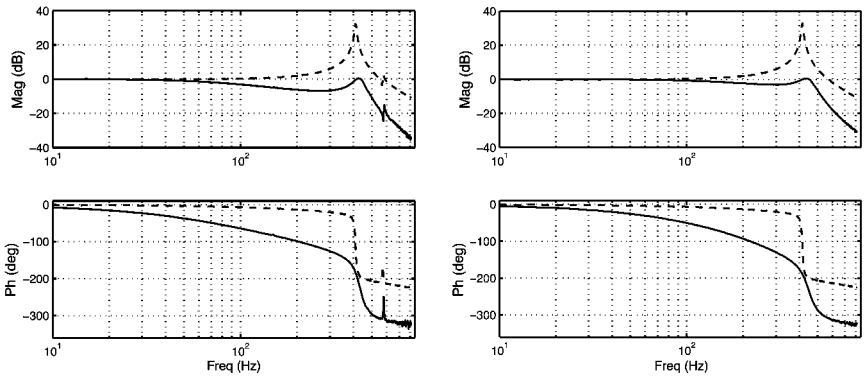

Fig. 10. Open-loop ($- - -$) and closed-loop (_____) polynomial-based controller+integral control frequency responses of the (a) X and (b) Y axes of the nanopositioning platform.

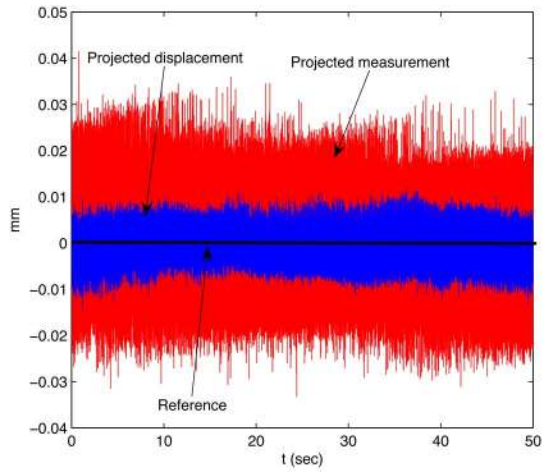

Fig. 11. Simulated system response $y(t)$, (35), and measured system response with the reference $r(t)$ being set to zero.

adequate gain and phase margins for both axes. Fig. 10 plots the experimentally measured open- and closed-loop polynomial-based controller+integral controller frequency responses for both the axes of the nanopositioning platform.

As mentioned in Section IV-A, due to the feedback of the sensor noise, the system output $y(t)$, (35), is not deterministic but random. Having fixed $C_1(s)$ and $C_2(s)$ for both the axis, the variance of the respective outputs can be empirically determined using the scheme presented in Section IV-A. Avoiding the details involved in calculating $\hat{S}_n(i\omega_k)$, $G_n(i\omega_k)$, and $\hat{S}_{y_n}(i\omega_k)$, the empirical values of the variances along the x and y axes are directly presented. The variances are

$$\sigma^2_{x,y_n} \approx 1.6355 \times 10^{-5}\ \mu\text{m}^2 \tag{46}$$

and

$$\sigma^2_{y,y_n} \approx 1.6230 \times 10^{-5}\ \mu\text{m}^2 \tag{47}$$

along the x and y axis respectively. The details involved in computing these variances are straightforward but tedious.

For illustration purposes, in Fig. 11, a simulated system response $y(t)$, along the x axis, and its projected measurement $y_m(t)$ are plotted. Here, $y(t)$, (35), is computed using Matlab with the reference $r(t) = 0$ and $n(t)$ being the noise realization plotted in Fig. 8, and $y_m(t) = y(t) + n(t)$. It is apparent form the plot that $y(t)$ is less noisier than $y_m(t)$. Thus, validating the fact that the actual system output is less noisy than the observed output, which is also evident from the values calculated for the variances σ^2_n, (37), and σ^2_{x,y_n}, (46).

Though this paper concentrates on large scan sizes (100 μm$\times$ 100 μm), there is significant interest in techniques that provide high-resolution images for small scan-sizes [31]. The technique presented here can easily be modified to deliver high-resolution small scans with minimal changes. The main constraint in this control scheme is the quantization noise introduced by the ADC/DAC boards. Very low noise, high gain preamplifiers can be used to amplify the sensor outputs so that the full range of the ADC /DAC boards can be utilized for small sensor outputs (corresponding to small scan sizes). 32-bit ADC/DAC systems that give subnanometer resolutions have already been used in nanopositioning applications [22]. Research on improved data acquisition systems for high-speed atomic force microscopy is also being carried out and will help greatly in enhancing the performance of existing control strategies [32].

It is apparent from (35) that by suppressing $Y_n(s)$, i.e., suppressing the magnitude of $G_n(i\omega)$ in (40), the noise response can be improved. However, the transfer-functions related to $Y_r(s)$ and $Y_n(s)$ are directly linked and they do not add up to one. Therefore, they cannot be treated as standard sensitivity and complementary sensitivity functions. Here, we just state that having a feedback controller comes at a cost, which is the noise response $Y_n(s)$.

A. Open- and Closed-Loop Hysteresis and Creep Evaluation

To test that the tracking action imparted by the integral controller does indeed eliminate nonlinear effects due to hysteresis, the system was excited by a 4 Hz 80 V sine wave. The platform input u plotted against the measured displacement output d (as denoted in Fig. 2) gives the total deviation from the desired trajectory; the hysteresis loop of the system. Fig. 12(a) shows the open-loop hysteresis plot. For the closed-loop system, the integral control forces the system to follow the input command, as shown in Fig. 12(b). It is clear that the closed-loop

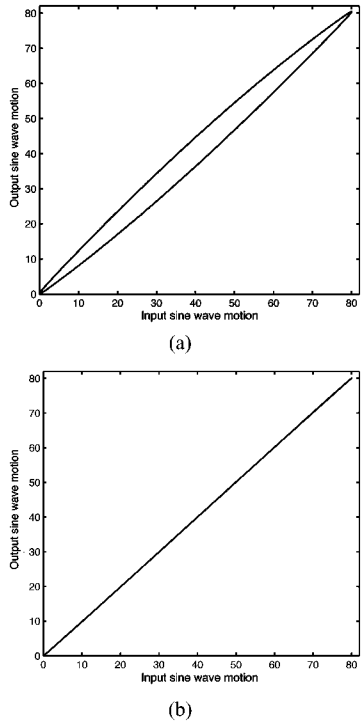

Fig. 12. (a) Open-loop and (b) closed-loop hysteresis plots for the nanopositioning platform. Using the notation given in Fig. 2, u is a 80 V, 4 Hz sine wave and d is the platform displacement in μm.

control scheme eliminates the nonlinear hysteresis effects almost totally. Thus, this control scheme effectively eliminates the two main problems associated with piezo-driven nanopositioning platforms: resonance and hysteresis.

An abrupt change in applied voltage does not produce an instantaneous and accurate change in the dimension of the piezoelectric stack actuator. This effect is known as creep and is the other main nonlinearity associated with piezoelectric elements. The effect creep has on scanning performance is that at two different scan speeds, it produces scans of different magnifications. An open-loop solution is to apply a voltage in the other direction that counteracts creep. Due to the tracking provided by the integral control, the effect of creep can be eliminated in closed loop. To test the performance of the open-loop and closed-loop system for creep, the system is commanded to move instantaneously by 20 μm from its zero initial position at $t = 10$ s. Fig. 13 shows the output displacement response of the open-loop and closed-loop nanopositioning platform from 0 s to 100 s. The gains for the open-loop and the polynomial-based controller-damped closed-loop match the gains shown by their respective magnitude plots shown in Figs. 3 and 9. As seen clearly, the integrator has eliminated creep for all practical purposes.

B. Raster Scan Results

A synchronized 4 Hz triangle wave and a staircase waveform were generated to produce the desired raster scan. This 4 Hz triangle wave, see Fig. 14(a), is used as input for one axis. It is seen that this input is capable of exciting the resonant mode of the respective axis which in turn introduces high-frequency harmonic distortion at the output, see Fig. 14(b). Also, as the

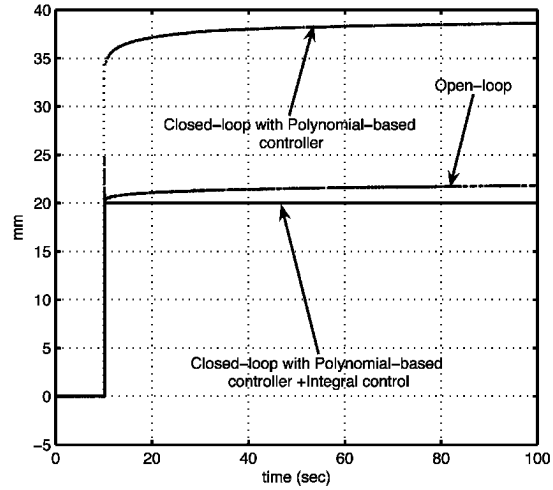

Fig. 13. Open-loop ($---$), polynomial-based controller-damped closed-loop ($\cdots$) and polynomial-based controller+integrator closed-loop ($\_\_\_\_\_$) platform displacement d, where u is a 20 V step command at $t = 10$ s. The notations u and d are consistent with those given in Fig. 2.

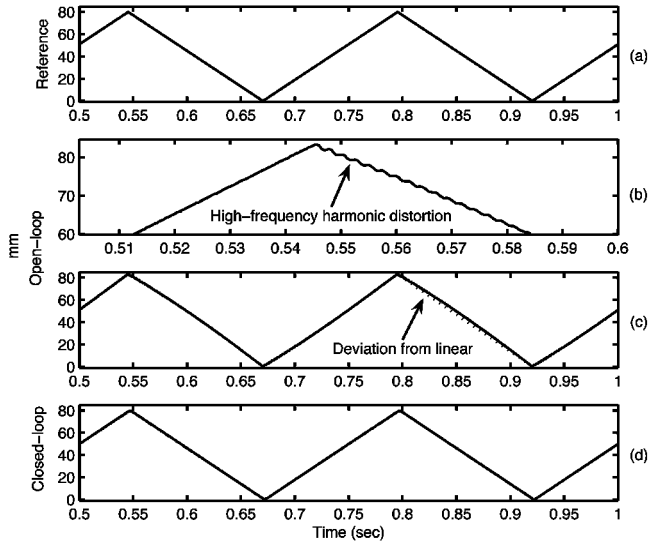

Fig. 14. (a) Reference 4 Hz 80 μm triangle scan. (b) Harmonic distortion due to excitation of resonant mode in open-loop. (c) Complete open-loop scan showing the nonlinear trace due to hysteresis. (d) Closed-loop triangle scan free from errors due to resonance and nonlinearities.

scan is over a sufficiently large range (80 μm), the deviation from linear of the obtained scan, due to hysteresis present in the stack actuator is also evident, see Fig. 14(c). The polynomial-based controller damps the resonant mode and the integrator effectively tracks the 4 Hz input triangle to result in a perfect triangle trace given in Fig. 14(d).

The second axis is given a staircase input. Fig. 15 shows the reference input, open-loop output and closed-loop output staircase traces. The open-loop nanopositioning platform does not follow the staircase input effectively as seen in Fig. 15(b). With the integral control forcing the nanopositioning platform to track the staircase input, the closed-loop trace is improved greatly as can be seen in Fig. 15(c). The superimposed sensor noise is clearly visible in these plots.

The plots presented in Figs. 14 and 15 are essentially measurements of the output $y(t)$, (35), along the x and y axes respectively. Plots in Fig. 14 are measurements of $y(t)$ with

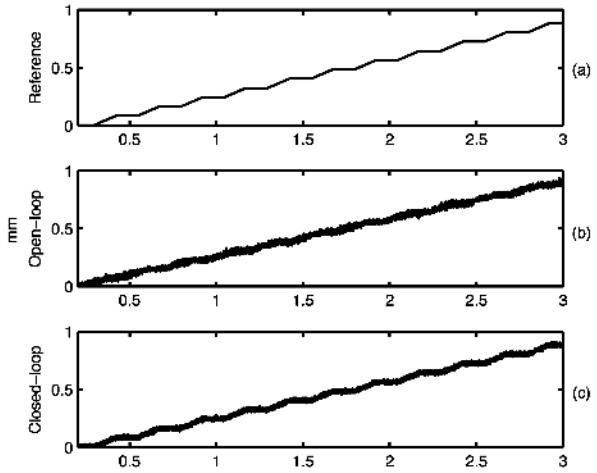

Fig. 15. (a) Reference staircase. (b) Staircase traced in open-loop. (c) Staircase traced in closed-loop.

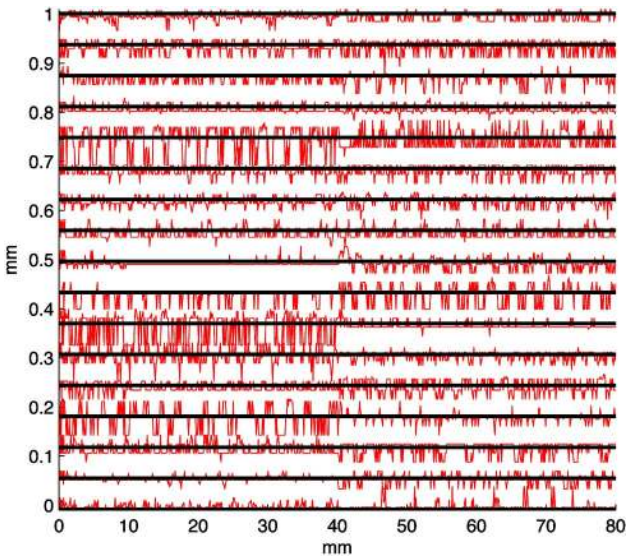

Fig. 16. Measured scan lines (faint) and scan lines obtained using the Kalman estimate (dark) at 62.5 nm from each other.

the reference $r(t)$ being a triangular waveform, while plots in Fig. 15 are measurements of $y(t)$ with $r(t)$ being a staircase. It is worth noting that $y(t)$ is a random variable. Moreover, as the plots are sensor measurements, they are essentially a realization of the random variable $y(t) + n(t)$. The presence of noise, though not apparent in the plots of Fig. 14 due to its larger scale, is fairly evident in the plots presented in Fig. 15. The measured scan lines of the traced raster pattern are presented in Fig. 16. The lines are 62.5 nm apart. It is apparent that the measured scan lines are noisy. The noise being both due to feedback and measurement. The empirical variances given in (46) and (47), imply that the standard deviations σ_{x,y_n} and σ_{y,y_n} are about 4 nm along both the x and y axes. This suggests that the adjacent scan lines in the raster pattern have to be at least 8 nm apart, which is twice the standard deviation. Otherwise, the chances of two adjacent scan lines overlapping becomes large, leading to poor image quality and reproducibility. With this resolution of 8 nm, 12500 scan lines can be produced in a 100 μm scan. In Fig. 16, the scan lines are 62.5 nm apart, which is about 15 times the standard deviation. A Kalman estimate of the output $y(t)$ is also plotted. It is apparent that the Kalman estimate of the scan is close to the desired scan.

VI. Conclusions

After comparing the closed-loop noise profiles of three damping controller designs (PPF, polynomial-based controller, and resonant controller), the polynomial-based controller was identified as the most suitable option for nanopositioning. The implemented polynomial-based controller damps the dominant first resonant mode of the nanopositioning platform by 23 dB. It was further shown that by combining this damping technique with an integral controller, nonlinear effects due to hysteresis and creep are minimized and superior tracking performance is achieved. This was demonstrated by tracing a 4 Hz 80 μm$\times$ 80 μm raster scan with a resolution of 62.5 nm. Noise analysis suggests a resolution of 8 nm is achievable.

Acknowledgment

The authors would like to thank D. Lockhard and I. Mahmood for their contributions.

References

[1] I. Fujimasa, *Micromachines: A New Era in Mechanical Engineering*. Oxford, U.K.: Oxford Univ. Press, 1996.
[2] B. Bhushan, *Handbook of Micro/Nanotribology*, 2nd ed. Boca Raton, FL: CRC, 1999.
[3] T. A. Desai, W. H. Chu, J. K. Tu, G. M. Beattie, A. Hayek, and M. Ferrari, "Microfabricated immunoisolating biocapsules," *Biotechnol. Bioeng.*, vol. 57, pp. 118–120, 1998.
[4] B. Bhushan, Ed., *Handbook of Nanotechnology*. New York: Springer, 2004.
[5] T. R. Hicks and P. D. Atherton, *The Nanopositioning Book: Moving and Measuring to Better Than a Nanometer*. London, U.K.: ISTE, 2000.
[6] G. Binnig, "The scanning tunneling microscope," *Sci. Amer.*, vol. 253, pp. 50–56, 1986.
[7] G. Binnig and D. P. E. Smith, "Single-tube three-dimensional scanner for scanning tunneling microscopy," *Rev. Sci. Instrum.*, vol. 57, pp. 1688–1689, 1986.
[8] B. Kang and J. K. Mills, "Vibration control of a planar parallel manipulator using piezoelectric actuators," *J. Intell. Robotics Syst.*, vol. 42, no. 1, pp. 51–70, 2005.
[9] A. J. Fleming and S. O. R. Moheimani, "Sensorless vibration suppression and scan compensation for piezoelectric tube nanopositioners," *IEEE Trans. Contr. Syst. Tech.*, vol. 14, no. 1, pp. 33–44, Jan. 2006.
[10] D. Niederberger, A. J. Fleming, S. O. R. Moheimani, and M. Morari, "Adaptive multimode resonant piezoelectric shunt damping," *Smart Mater. Struct.*, vol. 18, no. 2, pp. 291–315, Oct. 2004.
[11] G. Schitter, P. Menold, H. Knapp, F. Allgower, and A. Stemmer, "High performance feedback for fast scanning atomic force microscopes," *Rev. Sci. Instrum.*, vol. 72, no. 8, pp. 3320–3327, 2001.
[12] T. Ando, N. Kodera, D. Maruyama, E. Takai, K. Saito, and A. Toda, "A high-speed atomic force microscope for studying biological macromolecules in action," *Jpn. J. Appl. Phys.*, vol. 41, no. 7B, pp. 4851–4856, 2002.
[13] N. Kodera, H. Yamashita, and T. Ando, "Active damping of the scanner for high-speed atomic force microscopy," *Rev. Sci. Instrum.*, vol. 76, no. 5, pp. 1–5, 2005.
[14] H. R. Pota, S. O. R. Moheimani, and M. Smith, "Resonant controllers for smart structures," *Smart Mater. Struct.*, vol. 11, no. 1, pp. 1–8, 2002.
[15] G. C. Goodwin, S. F. Graebe, and M. E. Salgado, *Control System Design*. Englewood Cliffs, NJ: Prentice-Hall, 2001.
[16] J. L. Fanson and T. K. Caughey, "Positive position feedback control for large space structures," *AIAA J.*, vol. 28, no. 4, pp. 717–724, 1990.
[17] B. Bhikkaji, M. Ratnam, A. J. Fleming, and S. O. R. Moheimani, "High-performance control of piezoelectric tube scanners," *IEEE Trans. Control Syst. Technol.*, vol. 15, no. 5, pp. 853–866, Sep. 2007.

[18] S. O. R. Moheimani, B. J. G. Vautier, and B. Bhikkaji, "Experimental implementation of extended multivariable PPF control on an active structure," *IEEE Trans. Control Syst. Technol.*, vol. 14, no. 3, pp. 443–455, May 2006.
[19] M. Tsai and J. Chen, "Robust tracking control of a piezoactuator using a new approximate hysteresis model," *J. Dyn. Syst., Meas., Control*, vol. 125, pp. 96–102, Mar. 2003.
[20] A. Visintin, *Differential Models of Hysteresis*. New York: Springer-Verlag, 1996.
[21] H. Jung, J. Y. Shim, and D. Gweon, "Tracking control of piezoelectric actuators," *Nanotechnology*, vol. 12, pp. 14–20, 2001.
[22] A. Sebastian and S. M. Salapaka, "Design methodologies for robust nano-positioning," *IEEE Trans. Control Syst. Technol.*, vol. 13, no. 6, pp. 868–876, Nov. 2005.
[23] D. Croft, G. Shedd, and S. Devasia, "Creep, hysteresis, and vibration compensation for. piezoactuators: Atomic force microscopy application," *J. Dyn. Syst., Meas., Control*, vol. 123, no. 1, pp. 35–43, Mar. 2001.
[24] K. K. Leang and S. Devasia, "Iterative feedforward compensation of hysteresis in piezo positioners," in *Proc. 42nd IEEE Conf. Decision Control*, 2003, vol. 3, pp. 2626–2631.
[25] B. Graffela, F. Muller, A.-D. Muller, and M. Hietschold, "Feedforward correction of nonlinearities in piezoelectric scanner constructions and its experimental verification," *Rev. Sci. Instrum.*, vol. 78, 2007.
[26] O. M. El-Rifai and K. Youcef-Toumi, "Creep in piezoelectric scanners of atomic force microscopes," in *Proc. Amer. Control Conf.*, 2002, pp. 3777–3782.
[27] "PI-734 datasheet," in *Physik Instrumente Catalogue*, 2006.
[28] T. McKelvey, H. Akcay, and L. Ljung, "Subspace based multivariable system identification from frequency response data," *IEEE Trans. Autom. Control*, vol. 41, no. 7, pp. 960–978, Jul. 1996.
[29] R. G. Brown and P. Y. C. Hwang, *Introduction to Random Signals and Applied Kalman Filtering*. New York: Wiley, 2002.
[30] D. Croft, S. Stilson, and S. Devasia, "Optimal tracking of piezo-based nanopositioners," *Nanotechnology*, vol. 10, no. 2, pp. 201–208, Jun. 1999.
[31] A. A. G. Requicha, S. Meltzer, F. P. T. Arce, J. H. Makaliwe, H. Sikén, S. Hsieh, D. Lewis, B. E. Koel, and M. E. Thompson, "Manipulation of nanoscale components with the afm: Principles and applications," in *Proc. 1st IEEE Conf. Nanotechnol.*, 2001, pp. 81–86.
[32] G. E. Fantner, P. Hegarty, J. H. Kindt, G. Schitter, G. A. G. Cidade, and P. K. Hansma, "Data acquisition system for high speed atomic force microscopy," *Rev. Sci. Instrum.*, vol. 76, p. 026118, 2005.

Sumeet S. Aphale received his Ph.D. in Electrical Engineering from the University of Wyoming, Laramie, in 2005.

In 2005, he joined the University of Newcastle/ARC Center of Excellence, Callaghan, NSW, Australia, for Complex Dynamic Systems and Control as a Research Associate in Mechatronics. His research interests include vibration control, smart structures, nanopositioning and robotics.

Bharath Bhikkaji received the Ph.D. degree in signal processing from the Uppsala University, Uppsala, Sweden, in the year 2004.

He is currently a Research Academic at the School of Electrical Engineering and Computer Science, University of Newcastle, Callaghan, Australia. His research interests include system identification, robust control, and active noise and vibration control of flexible structures.

S. O. Reza Moheimani received the Ph.D. degree in Electrical Engineering from University of New South Wales at Australian Defense Force Academy, Canberra, Australia, in 1996.

Since 1997 he has been with the University of Newcastle, Callaghan, Australia, where he is a Professor with the School of Electrical Engineering and Computer Science. He also serves as the Assistant Dean (Research) for the Faculty of Engineering and an Associate Director of the ARC Centre for Complex Dynamic Systems and Control, an Australian Government Centre of Excellence. He is an Associate Editor of several international journals, and has chaired a number of international workshops and conferences. He has published two books, several edited volumes, and over 150 refereed articles. His current interests include applications of control and estimation in nanoscale positioning systems for scanning probe microscopy, control of electrostatic microactuators in MEMS, and data storage systems.

Prof. Moheimani is a co-recipient of 2007 IEEE TRANSACTIONS ON CONTROL SYSTEMS Technology Outstanding Paper Award.